processes

MDPI

Article

Reservoir Characteristics and Diagenetic Evolution of Lower Cretaceous in Baibei Sag, Erlian Basin, Northern China

Hongwei Tian [1], Zhanli Ren [1,2,*], Kai Qi [1], Jian Liu [1], Sasa Guo [1], Zhuo Han [1], Juwen Yao [1] and Lijun Zhu [1]

[1] Department of Geology, Northwest University, Xi'an 710069, China; tianhongwei1023@163.com (H.T.)
[2] State Key Laboratory of Continental Evolution and Early Life, Xi'an 710069, China
* Correspondence: renzhanl@nwu.edu.cn

Abstract: In recent years, the exploration of the Baibei Sag, located in the west of the Erlian Basin, has remained relatively underdeveloped. The Lower Cretaceous of the Baibei Sag hosts multiple tight sandstone reservoirs; however, research on the macro- and micro-characteristics, as well as the controlling factors of these reservoirs, is relatively limited. This study selected 105 Lower Cretaceous sandstone samples from the Baibei Sag for core observation, casting thin sections, scanning electron microscopy, X-ray diffraction, and high-pressure mercury intrusion analysis. The reservoir's physical properties, pore throat structure, and diagenesis process were studied. The results indicate that the reservoir lithology is mainly composed of feldspar lithic sandstone, with an average composition of 44.3% lithic, 34.6% quartz, and 21.2% feldspar. The clay minerals in the interstitial material are primarily illite (69.3%) and illite–smectite mixed layers (12.7%), with smaller amounts of chlorite (10.9%) and kaolinite (7.2%), while smectite content is very low. The physical property analysis results indicate that the average effective porosity of the Tengger Formation sandstone is 3.3%. The average permeability is 0.01×10^{-3} μm^2. The average effective porosity of the Aershan Formation sandstone is 0.86%, and the average permeability is 0.05×10^{-3} μm^2. The Tengger Formation and Aershan Formation are both tight sandstone reservoirs. The analysis of pore throat structure shows that the reservoir space is mainly composed of dissolution pores. Three types of pore throat structures were identified, and corresponding pore models were established. Based on burial history and organic matter evolution characteristics, this study establishes a diagenetic evolution sequence of the Lower Cretaceous sandstone reservoir. Analysis suggests that the pore throat structure of different reservoir types is mainly controlled by material composition. In the process of diagenetic evolution, the Tengger Formation and Aershan Formation are in the Middle diagenetic stage A. Compaction and cementation are the main reasons for low porosity, while the dissolution improves reservoir performance. The intergranular and intragranular dissolution pores formed by dissolution are the main storage spaces of the reservoir. The early tectonic fractures are filled with calcite, and the residual small-scale fractures play a role in improving permeability.

Keywords: Erlian Basin; diagenetic sequence; pore throat structure; reservoir characteristics

check for updates

Academic Editor: Qingbang Meng

Received: 1 April 2025
Revised: 28 April 2025
Accepted: 30 April 2025
Published: 2 May 2025

Citation: Tian, H.; Ren, Z.; Qi, K.; Liu, J.; Guo, S.; Han, Z.; Yao, J.; Zhu, L. Reservoir Characteristics and Diagenetic Evolution of Lower Cretaceous in Baibei Sag, Erlian Basin, Northern China. *Processes* **2025**, *13*, 1391. https://doi.org/10.3390/pr13051391

Copyright: © 2025 by the authors. Licensee MDPI, Basel, Switzerland. This article is an open access article distributed under the terms and conditions of the Creative Commons Attribution (CC BY) license (https://creativecommons.org/licenses/by/4.0/).

1. Introduction

The Erlian Basin is in the central eastern part of China and is one of the important oil and gas basins in China. In recent years, a series of achievements have been made in resource exploration in the Erlian Basin [1–8]. However, due to the complex geological structure of the Erlian Basin [9,10], there are significant differences in the scale of each

depression and the conditions for oil and gas accumulation. As one of the many oil and gas-bearing depressions in the Erlian Basin, the Baibei Sag has been studied by previous researchers for many years in terms of its tectonic characteristics, source rock characteristics, and reservoir characteristics [11–15]. However, previous research on reservoir characteristics has been limited to physical parameters such as porosity and permeability [12], and it is believed that the reservoirs belong to tight sandstone reservoirs. However, research on pore throat structure and formation reasons is still relatively limited, and this article focuses on this issue.

The physical properties of reservoirs are influenced by the interaction of reservoir material composition, diagenesis, and tectonic activity, which determine the physical properties of reservoirs by controlling their pore throat structure [16–18]. Tight sandstone reservoirs have extremely low porosity and permeability [19,20], small pore radius, poor connectivity, and strong heterogeneity. Therefore, the study of pore throat structure is of great significance for the study of reservoir characteristics in the study area. And diagenesis is an important factor affecting pore structure. Diagenesis mainly includes deep burial compaction and pressure solution, cementation and metasomatism, and dissolution, which control the evolution of pore throat structure [21–25].

This study collected sandstone samples from the Lower Cretaceous in the Baibei Sag of the Erlian Basin. Through core observation, combined with analysis and testing methods such as casting thin sections, scanning electron microscopy, X-ray diffraction, and high-pressure mercury intrusion, a detailed study was conducted on the composition, physical properties, and pore throat structure of the reservoir. The diagenesis process was analyzed to further explore the influencing factors of reservoir properties and pore throat structure. Based on burial history and organic matter evolution characteristics, the diagenetic evolution sequence of the Lower Cretaceous sandstone reservoir and different types of reservoir pore models were established.

2. Geological Setting

The Erlian Basin is one of the largest continental sedimentary basins in China. During the Late Jurassic and Early Cretaceous, the Erlian Basin witnessed the crustal extension and formed a series of faulted lake basins [26,27]. It is situated on the Hercynian fold basement of Inner Mongolia's Daxinganling and is a rift basin dominated by Lower Cretaceous strata. The Baibei Sag is located in the northeast of the Chuanjing Depression of the Erlian Basin. This Sag is a narrow strip, extending nearly east–west, with an area of approximately 1080 km^2 [11]. On the plane, the Baibei Sag can be divided into eastern and western structural zones, which are further subdivided into nine secondary structural units [12] (Figure 1).

The Baibei Sag is a Mesozoic sedimentary rift zone controlled by two first-order sequence boundaries [13]. Like other depressions in the Erlian Basin, the basement consists of a structural layer composed of hard sandstone, carbonate rock, flysch, and pyroclastic rock from Paleozoic and older strata. The overlying cover is composed of sandy conglomerate, volcanic rock, and coal- and oil-bearing strata from the Cretaceous and Cenozoic. The Lower Cretaceous is the primary oil-bearing formation, represented by a small continental faulted basin with a narrow east–west orientation, bounded by faults to the north and south. From top to bottom, the strata of the Baibei Sag are divided into the Erlian Formation (K_2e), the Saihan Formation (K_1s), the Duhongmu Formation (K_1d_1, K_1d_2, and K_1d_3), the Tengger Formation (K_1t), the Arshan Formation (K_1a_1 and K_1a_2), and the metamorphic basement (Figure 1). This study primarily focuses on K_1t and K_1a of the Lower Cretaceous sandstone reservoirs.

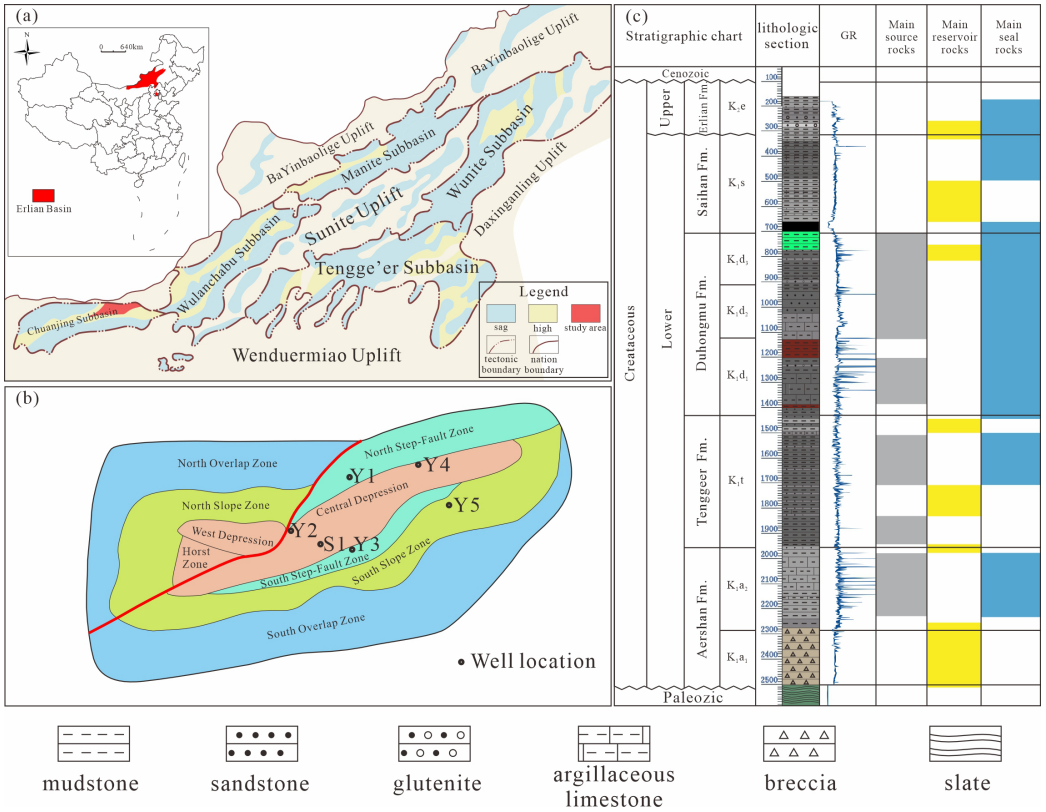


Figure 1. (**a**,**b**) Location and well location of the Baibei Sag. (**c**) Comprehensive histogram of lithology of the Baibei Sag. The colors in lithologic section show the main colors of the strata.

3. Materials and Methods

The samples in this study were collected from Lower Cretaceous core samples from five wells in the Baibei Sag, Erlian Basin. The locations of these wells are shown in Figure 1. Core observations were conducted to analyze the lithology and sedimentary facies characteristics of the sandstone reservoirs in the study area. The material composition of the samples was determined using cast thin sections (CTSs) and X-ray diffraction. The micro-morphology of the minerals was analyzed through scanning electron microscopy, and the diagenesis and diagenetic sequence were further examined. Physical properties, including porosity and permeability, were assessed through physical property tests, while the pore throat characteristics and distribution patterns were analyzed in conjunction with high-pressure mercury injection (HPMI) tests. Based on the results, the controlling factors of reservoir physical properties in the study area were also examined.

A total of 19 cast thin sections were prepared from the core samples. According to the Chinese Standard SY/T 5368-2016 [28], the polarizing microscope DM4500P (from Leica, Wetzlar, Germany) was used to observe and identify all thin sections, studying their material composition, pore structure, and reservoir morphological characteristics. For X-ray diffraction analysis, 30 core samples were selected. In accordance with the Chinese Standard SY/T 5163-2010 [29], the D8 Discover X-ray diffractometer (from Bruker, Munich, Germany) was employed for analysis. The ambient temperature was 22 °C, and the relative humidity was 35%.

In the physical property tests, 19 sandstone core samples were selected to measure rock density, porosity, and permeability, providing key physical property parameters for the sandstone reservoirs in the study area. For the high-pressure mercury injection test, 15 sandstone samples were chosen, with a sample particle size of 20–30 mesh and an equilibrium time of 45 s. Following the Chinese Standard SY/T 5346-2005 [30], the tests

were conducted using the Autopore 9510 mercury injection instrument (from Micromeritics, Norcross, GA, USA), with an upper limit set at 200 MPa, corresponding to a pore throat radius of 0.004 μm.

Scanning electron microscopy (SEM) analysis was performed on 33 samples using the FESEM JSM-7500F scanning electron microscope (from JEOL, Tokyo, Japan). The tests were conducted at a temperature of 20 °C, a humidity of 50%, and a voltage of 20 kV. A total of 109 images were taken, allowing for detailed observation of the occurrence and relationships of the minerals. The X-ray diffraction analysis, cast thin section preparation, and physical property testing were carried out at the Deposition Laboratory of the CNPC North China Oilfield Exploration and Development Research Institute. The high-pressure mercury injection and SEM analyses were completed at the Petroleum Geological Analysis and Test Center of the Exploration and Development Research Institute of the Zhongyuan Oilfield Branch.

4. Results

4.1. Core Observation

4.1.1. Lithological Observation

The sandstone reservoirs in the study area primarily consist of sandstone, conglomerate, and limestone. The sandstone is mainly composed of gravelly sandstone, pebbly fine sandstone, and fine sandstone, with quartz as the dominant component, followed by feldspar. It exhibits argillaceous cementation, with sub-angular to sub-rounded particles and medium sorting. The conglomerate mainly comprises fine conglomerate and glutenite, with quartz as the primary component, followed by feldspar. The cementation is predominantly argillaceous, with slight gray matter content, and the particles are sub-angular with poor sorting. The gravel radius generally ranges from 1 mm to 3 mm. The limestone is predominantly marl, tight, and hard, with a high calcite content. The grain fragment in the limestone mainly includes quartz, feldspar, volcanic rock fragments, quartz rock fragments, mudstone fragments, and siliceous rock fragments. The mud has a crystalline structure, with patchy gray matter distributed evenly and locally containing bioclastic materials (Figure 2).

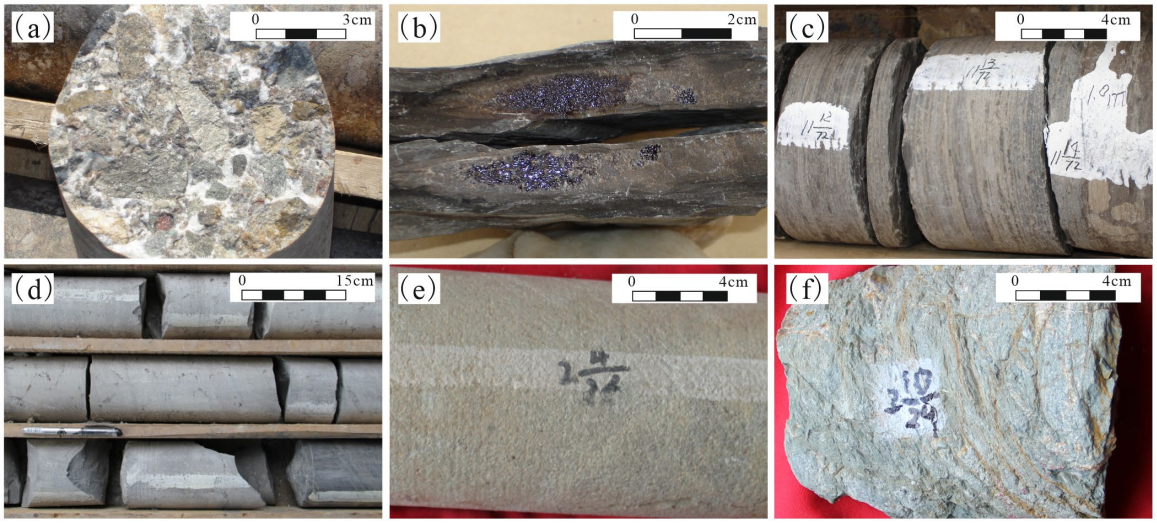


Figure 2. Lithological observation of the Baibei Sag: (**a**) gray white gravelly sandstone, from well S1, 2322 m, K_1a_1; (**b**,**c**) fluorescent-gray gray mudstone, from well S1, 1997.6 m, K_1a_2; (**d**) gray white lime mudstone, from well S1, 1010 m, K_1d_2; (**e**) light gray fine sandstone, from well Y2, 773.73 m, K_1t; (**f**) mottled mudstone, from well Y5, 811.7 m, K_1a.

4.1.2. Sedimentary Facies

According to the core data from well S1, the sedimentary facies of the Lower Cretaceous in the study area were analyzed. From top to bottom, the strata encountered in well S1 include Cenozoic, the Erlian Formation of the Upper Cretaceous, the Saihan Formation, the Duhongmu Formation, the Tengger Formation, the Arshan Formation (subdivided into the first and second members) of the Lower Cretaceous Baiyanhua Group, and the metamorphic basement.

Thick variegated breccia (Figure 3a) is developed in the first member of the Arshan Formation. The gravels are angular to sub-angular, with medium to poor sorting, and are filled with gray argillaceous silt. Based on the geological data of the study area, this member is interpreted as part of an alluvial fan sedimentary environment.

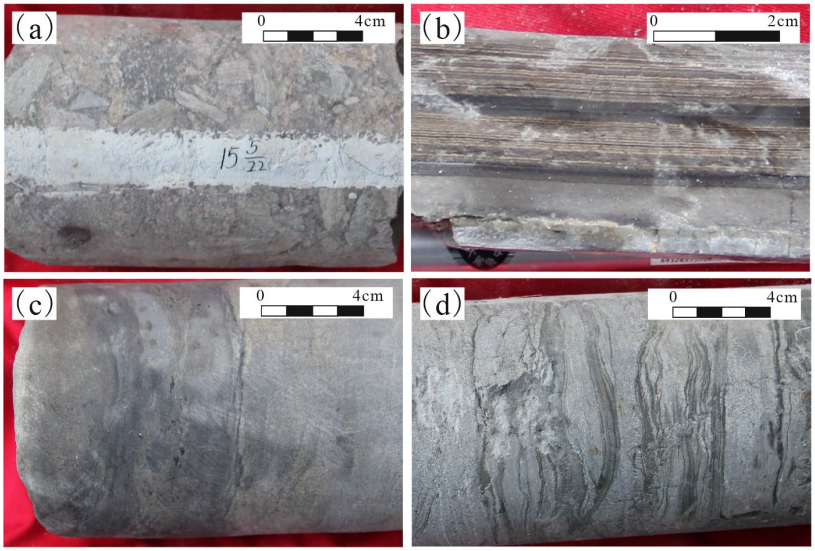


Figure 3. Sedimentary facies observation of the Baibei Sag: (**a**) mixed color breccia, from well S1, 2495 m, K_1a_1; (**b**) gray mudstone, from well S1, 2108 m, K_1a_2; (**c**) gray argillaceous siltstone, from well S1, 1734 m, K_1t; (**d**) gray siltstone, from well S1, 1533 m, K_1t.

Horizontal bedding (Figure 3b) is observed in the core of the second member of the Arshan Formation, with clear gray mudstone laminations. The development of horizontal bedding suggests a weak sedimentary hydrodynamic environment, typical of a deep lake to semi-deep lake setting.

The Tengger Formation is characterized by gray argillaceous siltstone (Figure 3c). The upper part consists of dark gray argillaceous siltstone, while the lower part is composed of gray siltstone. The laminae are unclear, and the bedding is gradual. Based on the geological characteristics of the study area, these features are interpreted as indicative of a deltaic sedimentary environment.

The Tengger Formation also includes gray siltstone (Figure 3d). The core reveals the development of corrugated cross-bedding, with grayish-green argillaceous laminations. The lithology is predominantly siltstone, and load structures are observed at the contact between the siltstone and mudstone, indicating a turbidite environment. This suggests possible deposition of a turbidite sand body.

4.2. Sandstone Petrology

4.2.1. Sandstone Composition and Texture

According to the observation of casting thin sections of sandstone core samples (Table 1), the sandstone samples in the study area are mainly composed of feldspar lithic sandstone (Figure 4), with an average terrigenous detrital composition of 44.3% lithic, 34.6% quartz, and 21.2% feldspar. The content of rock fragments varies greatly, ranging from 28% to 65%, mainly composed of metamorphic rock fragments (25.3%) and acidic ejected rock fragments (8.3%). The quartz content is between 19% and 41%; in the composition of feldspar (16%~35%), the content of alkaline feldspar is between 10%~21%, the content of plagioclase is between 6%~14%, and the content of impurities (fine-grained fillers) is relatively high (2%~31%), with an average of 13.3%. The content of impurities will affect the porosity, with a porosity of 0.5%~5% and an average porosity of 1.5%. The contact mode between particles is mainly point-line contact. The maturity of the sample structure is immature. The maturity of the ingredients ranges from 0.23 to 0.69, with an average of 0.54. Lower component maturity means higher content of feldspar and rock debris, with greater potential for secondary porosity. Under the action of dissolution, porosity can be significantly increased, especially during shallow burial stages (temperature < 80 °C) or under active fluid circulation conditions. A lower quartz content means that the sediment skeleton support is weaker and the compaction effect is more significant. Under compaction, plastic particles are more prone to deformation, rapidly reducing primary pores. And clay minerals are prone to water absorption and expansion during compaction, which can block pore throats.

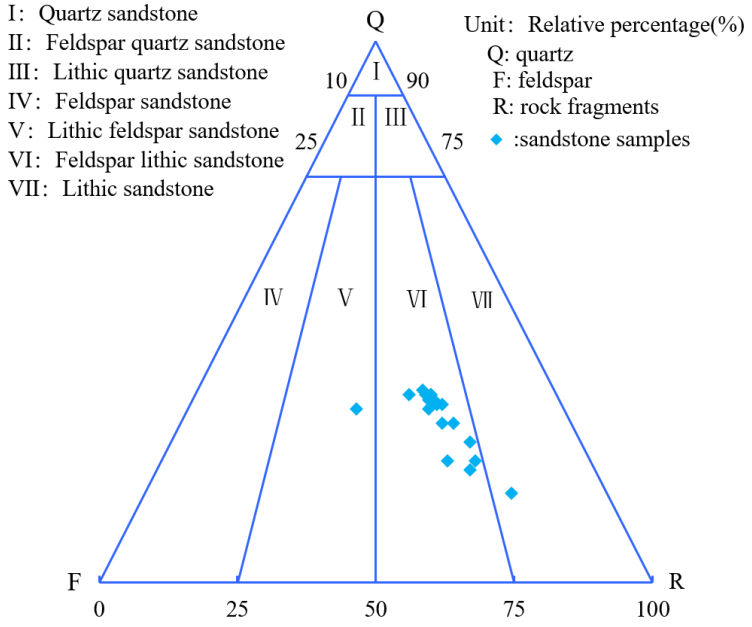


Figure 4. Composition diagram of Lower Cretaceous sandstone reservoir in the Baibei Sag.

Table 1. Deposit composition of the sandstone reservoir in the study area. RF: rock fragment.

Well	Depth (m)	Formation	Terrigenous Clast (%)	Terrigenous Clast (%)											Compositional Maturity
				Quartz	Feldspar		RF	Rock Fragments							
					Alkali Feldspar	Plagioclase		Volcanic Rock		Sedimentary Rock	Metamorphic Rock	Intrusive Rock	Tuff	Mica	
								Acid	Intermediate -Basic						
S1	1655.6	K_1t	85	19	10	6	65	7	2	15	23	16	2	<1	0.23
S1	1656.0	K_1t	81	26	12	7	55	10	1	8	26	7	3	<1	0.35
S1	1734.8	K_1t	88	37	21	14	28	5	0	0	20	0	2	1	0.59
S1	1735.9	K_1t	78	24	14	7	55	11	1	5	22	13	3	<1	0.32
S1	1736.8	K_1t	77	26	16	8	50	10	1	4	22	10	3	<1	0.35
Y1	749.1	K_1d_2	72	34	12	7	47	10	1	2	30	2	2	<1	0.52
Y2	775.2	K_1d_1	84	34	13	8	45	12	1	2	25	2	3	<1	0.52
Y2	778.4	K_1d_1	69	37	13	9	41	10	1	1	23	2	4	<1	0.59
Y2	778.6	K_1d_1	87	40	15	9	36	8	1	1	21	2	3	<1	0.67
Y2	1846.7	K_1t	83	39	13	8	40	7		0	29	2	2	<1	0.64
Y4	977.4	K_1t	69	38	12	8	42	10	1	3	23	2	3	<1	0.61
Y4	981.1	K_1t	76	30	11	7	52	11	1	8	26	3	3	<1	0.43
Y4	985.2	K_1t	71	38	12	7	43	10	1	2	25	2	3	<1	0.61
Y4	986.0	K_1t	66	40	12	8	40	11	<1	2	23	1	3	<1	0.67
Y5	1202.2	J	88	40	12	9	39	6	0	0	28	2	2	1	0.67
Y5	1202.6	J	84	39	12	8	41	6	0	0	30	2	2	1	0.64
Y5	1209.4	J	84	40	12	8	40	5	0	0	31	1	2	1	0.67
Y5	1401.8	J	86	41	12	9	38	5	0	0	29	1	2	1	0.69

4.2.2. Clay Mineral

The content of clay minerals significantly affects the physical properties of the reservoir. The clay mineral content ranges from 4% to 41%, with an average of 19.7%. The primary clay minerals are illite and I/S (illite–smectite mixed layers) (Figure 5). The illite content ranges from 41% to 83%, with an average of 69.3%. Illite is mostly in clastic particles and dissolution pores and takes on flake and filiform forms (Figure 6f,i). The illite content in the Tengger Formation increases with depth, while in the Arshan Formation, it decreases with depth. The content of I/S ranges from 5% to 45%, with an average of 12.7%, and is primarily distributed as sheets between pores (Figure 6i). The content of I/S in both the Tengger and Arshan formations decreases with depth. The chlorite content ranges from 3% to 19%, with an average of 10.9% (Figure 7f), and its content in the Tengger Formation increases with depth, while it decreases in the Arshan Formation. The kaolinite content ranges from 0% to 24%, with an average of 7.2%. The kaolinite content increases with depth in both the Tengger and Arshan formations, while smectite is almost absent in the reservoir.

From a vertical distribution perspective, as burial progresses, K^+ ions released from the dissolution of potassium feldspar promote the precipitation of illite in the alkaline pore water environment. The enhancement of deep diagenesis accelerates the transformation from smectite to illite. As depth increases, illite content in the Tengger Formation increases, while the content of I/S decreases, confirming this process. In the more deeply buried Arshan Formation, the transformation from smectite to illite is complete, and the content of I/S is further reduced. Additionally, under high-temperature and high-pressure conditions, the stability of illite decreases, and some illite is transformed into chlorite and other minerals. As depth increases, the illite content in the Arshan Formation decreases, while the chlorite content increases, supporting this process. The complete conversion of smectite to illite requires sustained temperatures (80~120 °C), adequate K^+ supply from internal mineral dissolution or external fluid influx, and adequate geological reaction time. It provides critical constraints on basin thermal history and fluid–rock interactions, aiding hydrocarbon exploration and reservoir quality prediction. The kaolinite content increases with depth, likely due to the enhanced dissolution of feldspar minerals by deep acidic fluids, such as CO_2 produced by the decarboxylation of organic matter. The dissolution of feldspar releases Al^{3+} and SiO_2, which preferentially form kaolinite under acidic conditions. The clay mineral content analysis suggests that both formations have undergone medium–deep diagenesis.

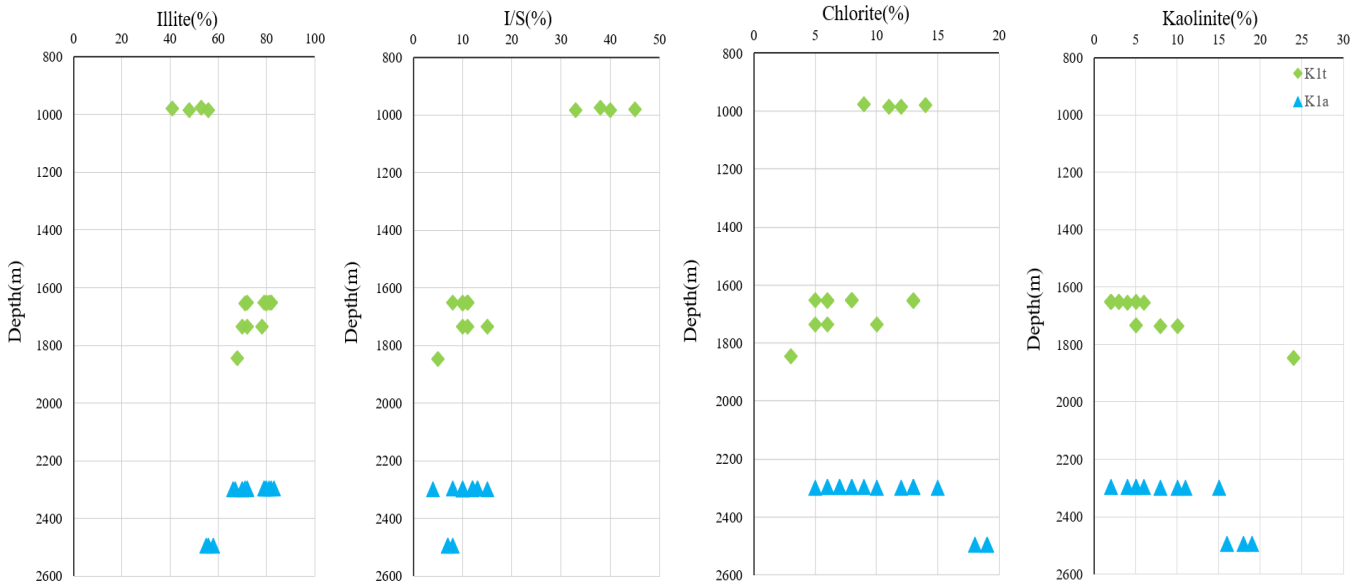


Figure 5. XRD data of lower Lower Cretaceous reservoir in the Baibei Sag.

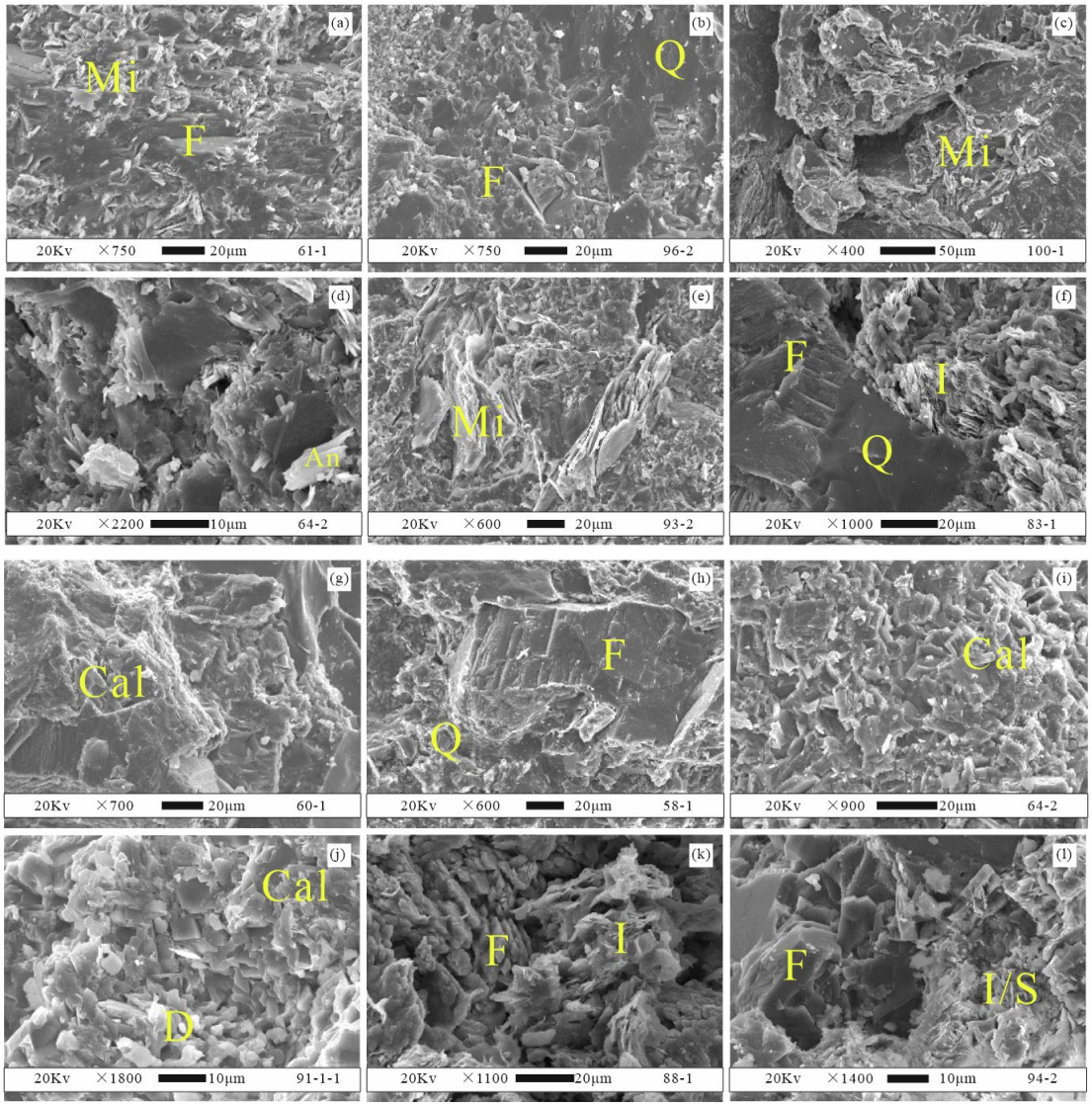


Figure 6. SEM observation. Mi: Mica, F: feldspar, Q: quartz, An: anhydrite, I: Illite, Cal: Calcite, D: dolomitic: (**a**) The feldspar surface is corroded and sericitized. Well S1, 1735 m. (**b**) The quartz particles are replaced by calcite. Well S1, 2297.85 m. (**c**) Intergranular pores and lamellar mica are altered. Well S1, 2494.5 m. (**d**) Dissolution micropores, pore size 1~2 μm, anhydrite columnar crystals can be seen. Well S1, 1736 m. (**e**) Flake mica is deformed due to compaction. Well S1, 2297.35 m. (**f**) Illite dissolution metasomatism quartz particles, visible dissolution pores, quartz, and potassium feldspar are pressure-embedded. Well S1, 2295.94 m. (**g**) Calcite crystal with a fine crystal structure of cement. Well S1, 1734.91 m. (**h**) Potassium feldspar particles and microcrystalline siliceous cements around them. Well S1, 1733.62 m. (**i**) Microcrystalline calcite crystals are mosaic. Well S1, 2296.93 m. (**j**) Microcrystalline iron dolomite crystal, iron dolomite replacement calcite. Well S1, 2297.2 m. (**k**) Potash feldspar is dissolved, with lamellar illite and slightly dissolved pores. Well S1, 2296.63 m. (**l**) Secondary albite crystal and lamellar I/S. Well S1, 2297.55 m.

Moreover, the smectite-to-illite reaction is temperature- and time-dependent. Shallower transitions indicate higher geothermal gradients or rapid burial (e.g., tectonic subsidence), while deeper transitions suggest slower burial or lower heat flow. In adjacent sags, variations in the depth of I/S illitization can highlight differences in thermal maturity. Moreover, the zones of advanced illitization may reflect K-rich fluid migration. Fluid chemistry inferred from I/S trends in one sag can predict diagenetic pathways in adjacent sags. Illite and I/S variations serve as proxies for thermal history and fluid interactions, enabling the predictive models of reservoir quality in adjacent sags.

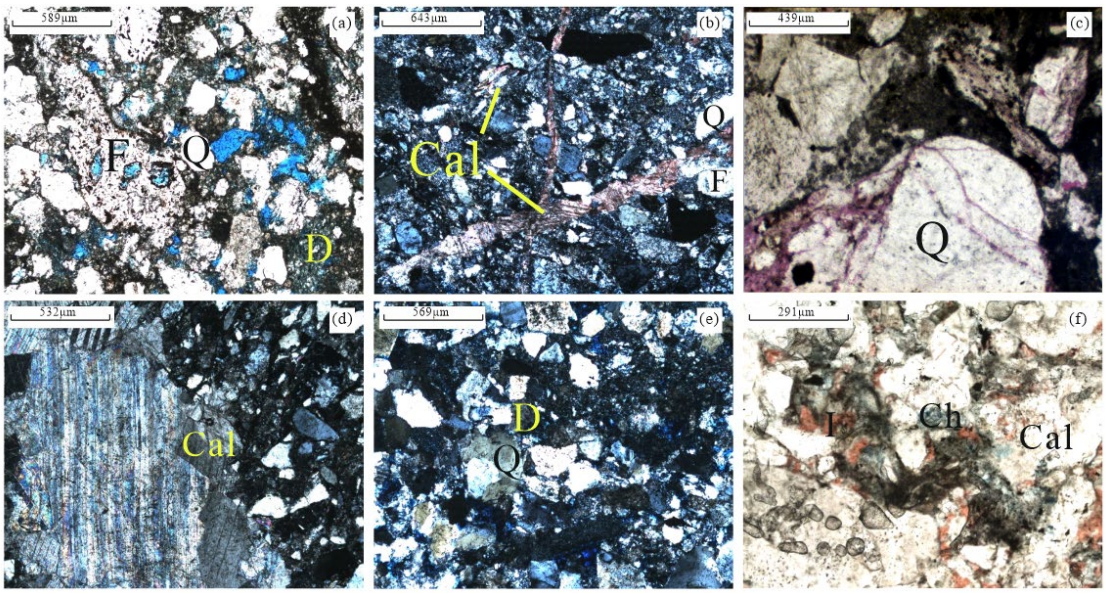


Figure 7. Cast thin sections for observation. F: feldspar, Q: quartz, D: dolomitic, Cal: Calcite, Ch: chlorite: (**a**) Authigenic dolomite filled the pores and metasomatized the matrix and particles, developed intergranular dissolved pores, feldspar fragment intragranular dissolved pores, and mold pores. Well Y2, 774 m. (**b**) Authigenic calcite fills the pores and metasomatizes the matrix and particles, and the structural fractures are nearly linear and filled with calcite. Well Y5, 1400.6 m. (**c**) Variegated breccia grain compaction crack, Well S1, 2013 m. (**d**) Unequal grain structure. Argillaceous matrix is mainly distributed among grains, and the matrix undergoes recrystallization to the illite phenomenon. A small amount of authigenic calcite filled the pores and replaced the matrix and particles. Fine intergranular dissolved pores and feldspar and fragment intracranular dissolved pores are locally developed with poor connectivity. Well S1, 1201.4 m. (**e**) A small amount of micrite dolomite sand fragment. Authigenic dolomite fills the pores and metasomatizes the matrix and particles, and quartz particles are generally secondarily enlarged. Well Y2, 777.4 m. (**f**) Authigenic illite and chlorite are distributed in the intergranular and grain edge, and authigenic calcite fills the intergranular and metasomatizes the grain and matrix. Well S1, 1654.4 m.

4.3. Reservoir Characteristics

4.3.1. Porosity and Permeability

The physical properties of the reservoir were analyzed for 36 samples from the study area (Figure 8). The results indicate that the rock density of the Tengger Formation sandstone reservoir ranges from 2.35 g/cm^3 to 2.73 g/cm^3, with an average density of 2.60 g/cm^3. The effective porosity ranges from 0.2% to 9.5%, with an average of 3.3%. The permeability ranges from 0.004×10^{-3} to 0.111×10^{-3} μm^2, with an average of 0.01×10^{-3} μm^2. For the Aershan Formation sandstone reservoir, the rock density ranges from 2.66 g/cm^3 to 2.73 g/cm^3, with an average of 2.69 g/cm^3. The effective porosity ranges from 0.2% to 2.2%, with an average of 0.86%, and the permeability ranges from 0.027×10^{-3} to 0.116×10^{-3} μm^2, with an average of 0.05×10^{-3} μm^2. Both the Tengger and Aershan formations are classified as tight sandstone reservoirs.

In terms of spatial distribution, the effective porosity of sandstone reservoirs in the Tengger and Aershan formations decreases significantly with depth, while changes in permeability are less pronounced. Several factors contribute to this observation: First, diagenetic processes such as structural fractures or dissolution may lead to the formation of micro-fractures (Figure 7c) or secondary pores (Figure 6d,f). Even if primary pores are reduced, the connectivity of secondary pores can maintain a certain level of permeability. Second, during diagenesis, cement tends to accumulate near particle contact points (Figure 6d), and most intergranular pores remain connected, thus preserving permeability

despite reduced porosity. Third, new minerals formed during cementation and metasomatism (Figure 6h) create a more stable supporting structure or increase the pore throat radius, helping to mitigate the negative impact of reduced pore volume on permeability.

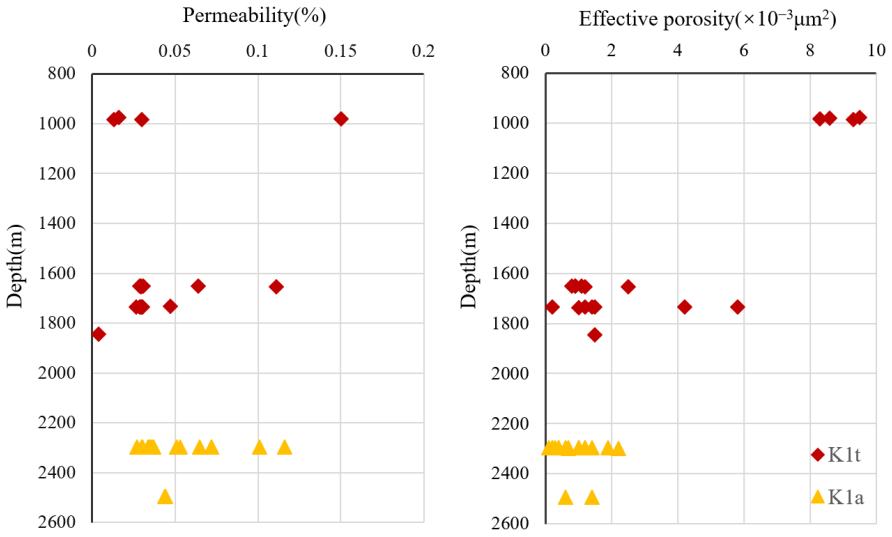


Figure 8. Relationship between permeability, effective porosity, and depth.

4.3.2. Pore Throat Types

Based on cast thin section and core observations, the storage space in the study area is primarily composed of dissolution pores, including intergranular dissolution pores, intragranular dissolution pores, and mold pores (Figure 7a). Intergranular dissolution pores are mainly formed along the edges of aluminosilicate minerals in feldspar and rock fragments, while intragranular dissolution pores and mold pores primarily develop within the interior of feldspar and rock fragment particles, exhibiting poor connectivity. Under scanning electron microscopy (SEM), the feldspar surface is eroded and sericitized (Figure 6a), and quartz particles are eroded and metasomatized by calcite (Figure 6b). The size of dissolution pores is primarily concentrated in the range of 10–40 μm, with a maximum pore size of 180 μm. The throat radius ranges from 3 to 5 μm, with a maximum of 15 μm. This suggests that aluminosilicate minerals (feldspar, rock fragment) have undergone dissolution by strong acidic fluids during diagenesis.

Under the microscope, nearly linear fractures are observed (Figure 7b), which are completely filled with calcite, indicating that the structural fractures underwent carbonate cementation after formation. This is associated with products of hydrothermal activity or pressure dissolution during deep burial. The alteration of lamellar mica is visible under SEM (Figure 6c), which may be related to the illitization process of K^+-rich fluids, reflecting changes in mineral stability with temperature and pressure conditions during diagenesis. Additionally, columnar anhydrite crystals are observed in the dissolution micropores (Figure 6d), indicating that secondary pores formed during early dissolution were later filled by calcite cementation, anhydrite precipitation, and other filling events, reflecting the characteristics of multi-stage diagenetic fluid superimposition and transformation.

4.3.3. Pore Throat Structure Characteristics

Previous studies have shown that the mercury saturation frequency and capillary pressure curve obtained from the HMIP test are controlled by the reservoir's pore throat structure. Based on the capillary pressure curves, mercury saturation frequencies, and relevant data, the sandstone samples in this study are categorized into three types. The corresponding data for each sample are listed in Table 2.

Table 2. HPMI data and classification of samples.

Sample ID	Depth	Formation	Average Throat Radius (μm)	Relative Sorting Coefficient	Sorting Coefficient of Throats	Displacement Pressure (MPa)	Type
1	1654.26	K_1t	0.5	0.17	2	0.73	1
2	1654.26	K_1t	1.69	0.23	2.16	0.18	1
3	1733.62	K_1t	0.01	0.29	3.54	29	3
4	1734.31	K_1t	0.79	0.17	1.77	0.45	1
5	1734.91	K_1t	0.79	3.22	3.22	0.29	2
6	1735	K_1t	1.36	0.36	3.16	0.29	1
7	1735.51	K_1t	0.24	0.38	3.61	1	2
8	1736	K_1t	0.02	0.36	3.96	18	3
9	2296.13	K_1a_2	0.83	0.19	2.09	0.45	1
10	2296.33	K_1a_2	0.33	0.28	2.63	0.73	1
11	2297	K_1a_2	0.03	0.46	4.6	11	3
12	2297.2	K_1a_2				0.45	2
13	2297.25	K_1a_2				0.5	2
14	2298.1	K_1a_2				0.45	2
15	2494.5	K_1a_1				1.1	2

For Type 1 samples, the displacement pressure is the lowest (0.18–0.73 MPa), with an average of 0.47 MPa, and the sorting of pore throat is the best (Figure 9(a1)). The pore throat radius is concentrated between 0.25 and 1.6 μm, with an average radius of 0.92 μm. The capillary pressure curve features a long, gentle section in the initial stage. As capillary pressure increases, the horizontal section of the invasion curve narrows (Figure 9(a2)). At a capillary pressure of 200 MPa, the mercury saturation is high (77.88–90.19%), with an average of 84.56%.

For Type 2 samples, the displacement pressure ranges from 0.29 to 1.1 MPa, with an average of 0.63 MPa. The sorting of pore throats is poor (Figure 9(b1)). The pore throat radius is concentrated between 0.01 and 1.4 μm, with an average radius of 0.51 μm. The capillary pressure curve is generally steep and uneven (Figure 9(b2)). At 200 MPa capillary pressure, the mercury saturation is high (72.45–92.63%), with an average of 83.51%.

For Type 3 samples, the displacement pressure is relatively high (11–29 MPa), with an average of 19.3 MPa. The sorting of pore throat is good; however, the pore throat radius is the smallest (Figure 9(c1)), ranging from 0.004 to 0.016 μm, with an average radius of 0.02 μm. The capillary pressure curve is generally gentle (Figure 9(c2)). At 200 MPa capillary pressure, the mercury saturation is the lowest (63.87–75.15%), with an average of 69.86%.

Among the three types of reservoirs, Type 1 exhibits concentrated large throat distribution, strong pore homogeneity, excellent pore throat connectivity, and high fluid seepage ability. In contrast, the two other reservoir types display significant differences in throat sizes. Type 2 and Type 3 reservoirs are characterized by strong heterogeneity in pore throat structure, poor pore throat sorting, and complex seepage paths. The pore throat of Type 3 reservoirs is well sorted but very fine, resulting in a highly dense pore throat structure. Mercury requires high pressure to enter the micro-throats, which results in very poor permeability. The HPMI test results systematically reveal the heterogeneity of pore throat structure and the differences in physical properties. Type 1 reservoirs have the advantage of a homogeneous, relatively large pore throat, while Type 3 reservoirs have become inefficient due to their extremely fine pore throats and poor connectivity. Type 2 reservoirs exhibit transitional characteristics. Vertically, the reservoirs in both the Tengger and Arshan formations contain all three types (1, 2, and 3), and the correlation between the distribution of reservoir types and depth is minimal.

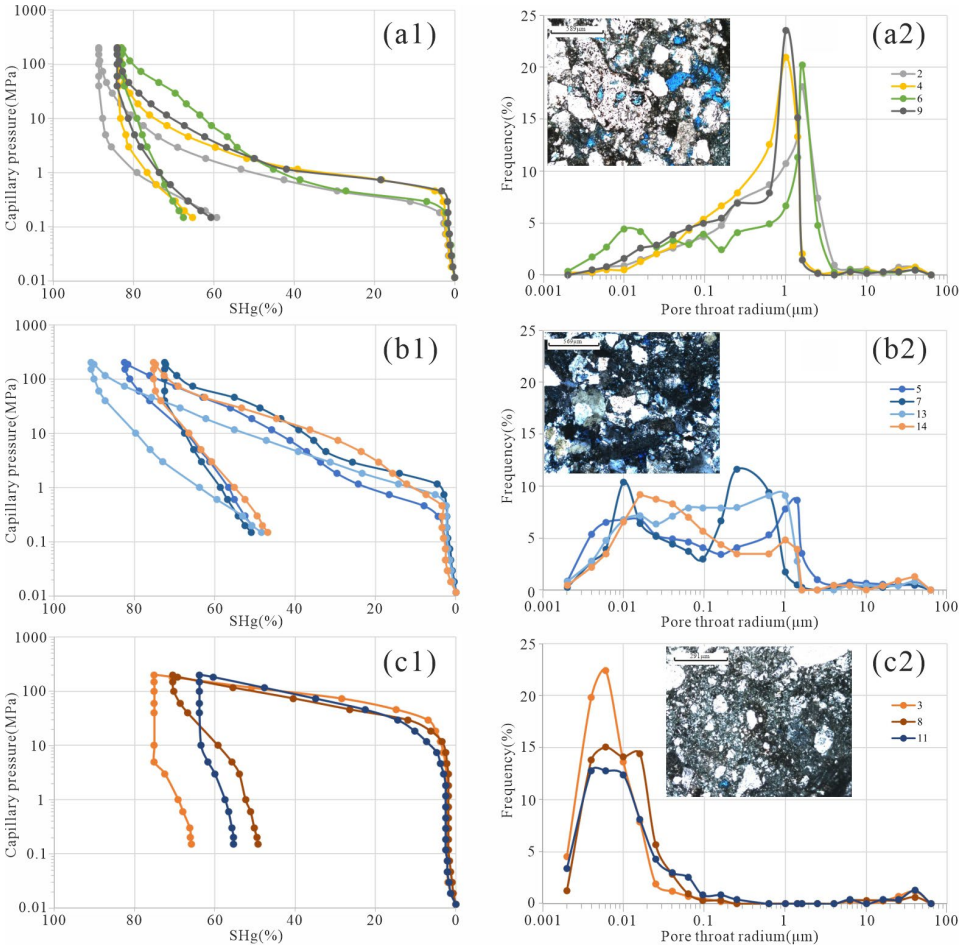


Figure 9. Capillary pressure curves of (**a1**) Type 1, (**b1**) Type 2, and (**c1**) Type 3, and distribution curves of pore throat ratios for (**a2**) Type 1, (**b2**) Type 2, and (**c2**) Type 3 of the sandstone reservoirs of the Baibei Sag.

5. Discussion

5.1. Type of Diagenesis

After burial, sediments undergo diagenetic transformations that alter their composition and structure, significantly impacting their storage space. Understanding diagenesis is essential for identifying the primary processes during reservoir burial and assessing the influence of various factors on reservoir space, which aids in predicting favorable reservoir development areas. In general, during diagenesis, compaction and cementation significantly reduce reservoir performance, while dissolution can enhance reservoir development to some extent [26,27].

5.1.1. Compaction

As sediments are buried, the increasing load and pressure from overlying sediments lead to changes in particle arrangement and contact modes, significantly reducing the volume of intergranular pores and sediments. Diagenetic fluids are expelled from the pores, resulting in a considerable reduction in primary porosity. Additionally, soluble substances in the sediment transform into clay minerals under high temperature and pressure, severely limiting the formation of secondary pores. Compaction also adversely affects fluid migration, thus hindering the dissolution process. Previous studies have shown that well-sorted sandstone can have an initial porosity of up to 40% [31] while the average porosity of samples in the study area is 2.1%. This study demonstrates that compaction is a significant factor contributing to low porosity in the study area.

Various factors influence the intensity and rate of compaction, including the composition of clastic particles, interstitial materials, diagenetic fluids, tectonic stress, and geothermal conditions [32–35]. As compaction progresses, clastic particles are compressed together, resulting in contact modes such as point, line, concave–convex, and even suture-line contacts. Compaction causes brittle particles, such as feldspar, quartz, and rock blocks, to fracture (Figure 7c), while opening along the cleavage of feldspar. Plastic particles, such as mica fragments and argillaceous and marly fragments, bend and deform under compaction (Figure 6e). Previous studies have shown that plastic particles deform under compaction, increasing porosity loss, while rigid particles resist compaction, aiding in the preservation of primary pores. Furthermore, compaction leads to lattice sliding in clastic particles like feldspar, resulting in the sliding deformation of their bicrystals.

In the tight sandstone reservoirs of the study area, concave–convex and suture-line contacts are observed even at shallow burial depths. When the burial depth reaches around 1500 m, mosaic contact between particles becomes evident (Figure 6f,i), indicating that the strata at this depth have experienced significant compaction. The impact of compaction on the reservoir also depends on the fabric characteristics of the reservoir itself. Well-sorted sandstones with high compositional and structural maturity are less affected by compaction.

5.1.2. Cementation

Carbonate cement can fully cement clastic particles and fill large intergranular spaces, which has a significant impact on reservoir performance [36–39]. Various types of cementation occur in the tight sandstone reservoirs of the study area, with carbonate mineral cementation being the most prominent (Figures 7f and 8). Siliceous cementation (Figure 6h), illite cementation (Figure 6f), anhydrite (Figure 6d), sulfate, kaolinite, and other cementations are also common. The type and strength of cementation significantly affect the reservoir performance, and these factors are controlled by the material composition of the tight sandstone reservoir.

The carbonate cementation in the study area includes the cementation and metasomatism of micrite carbonate minerals, early carbonate minerals, and late carbonate minerals. Micritic carbonate cements mainly consist of micritic calcite and dolomite, which are present in small amounts and are unevenly distributed. They typically occur in micritic or microcrystalline forms between clastic particles or in brittle fractures, and sometimes along cleavage fractures of mica fragments. Micritic carbonates are generally formed during the syngenetic stage or early diagenetic stage A, and during diagenesis, they are either eroded and metasomatized or slightly recrystallized, making them rare in the reservoir. Early carbonate cements are mainly calcite, with dolomite being less common (Figure 7e). The content of calcite varies widely in the reservoir, ranging from nearly absent to over 40%, typically about 5–20%. Dolomite generally accounts for less than 5% and is often involved in medium to strong cementation. The grain size of dolomite is generally smaller than that of calcite. Early carbonate minerals also have strong metasomatism towards quartz, feldspar, and rock debris during the cementation process. The metasomatic relationship between calcite and dolomite is not obvious, as they generally do not come into contact with each other; however, overall, dolomite should have formed slightly later than calcite. Early carbonate minerals generally form during the early diagenetic stage but have a strong impact on the pore space in the reservoir, particularly in strata such as the Tengger and Arshan formations. These minerals replace quartz and cement particles and can also locally replace late carbonate minerals.

Late carbonate cements include iron-bearing dolomite and iron-bearing calcite, primarily in the form of powdery and microcrystalline iron-bearing dolomite. These late carbonate minerals metasomatize clastic particles, including early carbonate minerals like

calcite (Figure 6j). The content of carbonate minerals is closely related to heterobase content, compositional maturity, and structural maturity. Carbonate cement has a dual impact on the reservoir: on one hand, it significantly reduces primary porosity and damages the physical properties of the reservoir, but on the other hand, it can hinder further compaction and reduce the degree of compaction. And due to its acid solubility, the pores occupied by carbonate minerals due to cementation can be released under appropriate conditions, thus acting as a favorable factor.

The siliceous cementation is mainly manifested in two forms: secondary quartz enlargement and authigenic quartz (Figure 6h). Quartz secondary enlargement is relatively small, becoming noticeable from about 400 m, with the enlarged edge typically reaching 0.02–0.03 mm. Authigenic quartz, which attaches to the pore wall, has a crystal radius of 10–25 μm and is present in small amounts, observable only with SEM. Quartz cement may come from the alteration and dissolution of rock fragments, in situ pressure dissolution, and transformation of clay minerals, with silicate mineral dissolution being the main source [40–42]. This indicates that the diagenesis in the study area has reached an advanced stage, and there was structural uplift in the later stage.

Clay minerals are often distributed between clastic particles in sandstone. The main diagenetic change in clay minerals inherited from the parent rock is recrystallization. Clay minerals formed during diagenesis can be identified using scanning electron microscopy. X-ray diffraction analysis shows that the clay minerals in the tight sandstone reservoirs are mainly illite, chlorite, and I/S (Figure 6i). Illite, which is flaky and filamentous, often forms clay bridges between particles. An important factor in the formation of authigenic illite is the illitization of smectite, which occurs at temperatures above 70–85 °C, accompanied by the albitization of potassium feldspar. The illitization process continues until smectite or potassium feldspar is completely depleted [43]. X-ray diffraction results indicate that smectite is nearly absent in the samples, with potassium feldspar content ranging from 1% to 6%, suggesting large-scale illitization of smectite in the study area. At temperatures exceeding 130 °C, kaolinite also transforms into illite. Previous studies have shown that the conversion of kaolinite to illite is controlled by the ratio of potassium feldspar to kaolinite [44,45]. The average kaolinite content in the samples is 7.2% (Figure 5), with most samples containing 2–4% potassium feldspar, indicating that kaolinite is slightly dominant in this transformation.

5.1.3. Dissolution

Dissolution is a widespread diagenetic phenomenon in the study area and plays a crucial role in enhancing reservoir physical properties [46–49]. Intergranular and intragranular dissolution pores are the primary reservoir spaces in the tight sandstone reservoirs. In the study area, quartz and feldspar dissolution is common (Figure 6a,b), with dissolution occurring along feldspar cleavage fractures, transforming feldspar into honeycomb or fragment-like structures (Figure 6k). Another soluble clastic component is rock fragment, which consists of micrite carbonate rock, phyllite, and schist. Some particles dissolve completely, forming mold holes and large particle voids. The Dissolution of intergranular cement is also common (Figure 6c).

Previous studies have shown that fluid properties and migration channels in the reservoir control the intensity of dissolution [50–52]. As organic matter and argillaceous material precipitate together, the increase in burial depth and thermal evolution leads to the production of organic acids, which selectively dissolve the rock. The reservoir in the study area is predominantly feldspathic lithic sandstone, and many intergranular pores are preserved from early diagenesis, aiding fluid migration and dissolution [34,52]. However, as compaction progresses, diagenetic fluids are expelled, and corrosion products become

trapped, leading to the formation of cements such as carbonate, clay, and silica [53–55] (Figure 6g,h), which limits the positive effects of dissolution on the reservoir.

5.2. Diagenetic Sequence

Based on microscopic observation and experimental analysis, combined with the organic matter evolution and stratigraphic burial history of the study area [14], and meeting the standard of Chinese petroleum and natural gas industry SY/T 5477-2003 [56], this article divides the diagenetic evolution stages (Figure 10). The Tengger Formation and Aershan Formation in the study area have reached the Middle diagenetic stage A through three processes: (1) from sedimentation to early Middle Cretaceous, rapid burial, strong compaction, and the influence of weakly acidic environments formed by organic matter hydrocarbon generation, corresponding to the early diagenetic stage. (2) From the Early Middle Cretaceous to the Late Cretaceous, the strata rapidly uplifted, compaction weakened, and structural fractures improved reservoir properties. Due to still being buried at a large depth, diagenetic evolution continued, corresponding to the middle diagenetic stage A. (3) From the end of the Cretaceous to the present, the tectonic activity in the study area has been stable, with weak sedimentation, and the diagenetic evolution has been maintained at the middle diagenetic stage A.

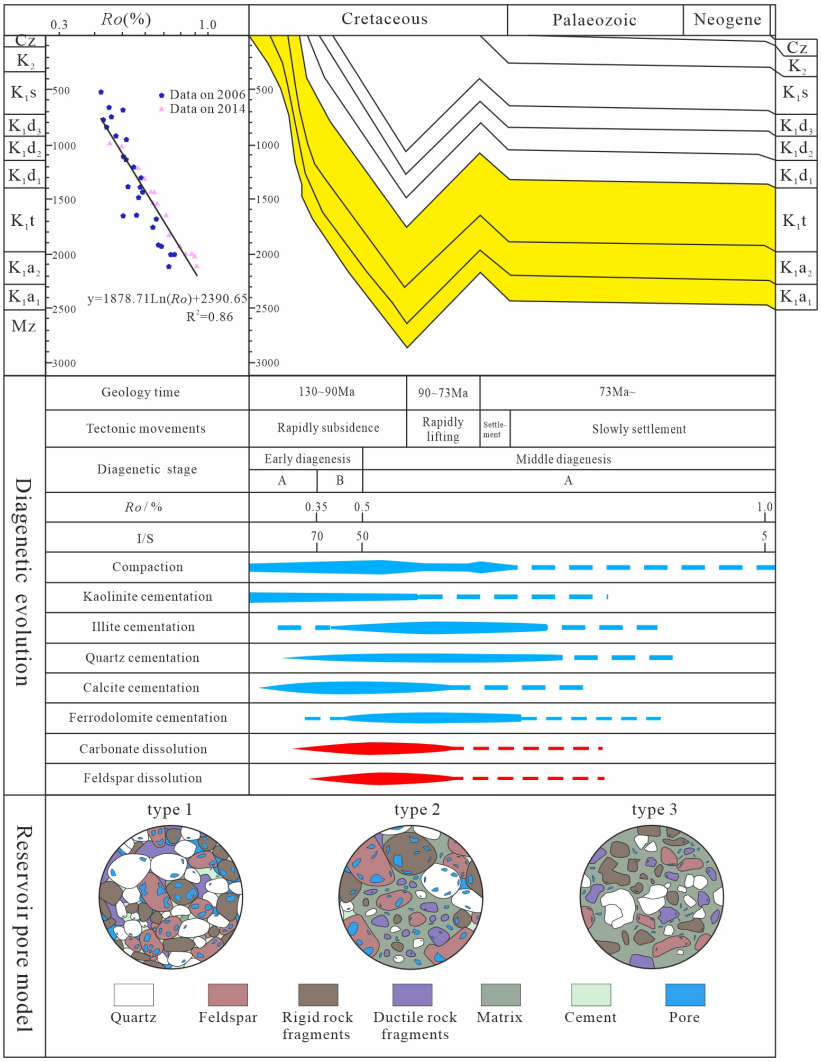


Figure 10. Classification of diagenetic evolution stages and reservoir pore model for sandstone reservoirs of the Baibei Sag. The sizes of different shapes in Diagenetic evolution reflect the strength of diagenesis. (burial history simulation and depth plots of Ro modified from Liu et al., 2018 [14]).

At the peak of oil generation, many organic acids are discharged from the source rock, and we believe that the reservoir currently has experienced the strongest dissolution. Due to the rapid burial rate, the compaction and cementation have not reached the strongest stage, which is conducive to oil and gas migration and reservoir reconstruction. However, the compaction and cementation since 100–73 ma have significantly damaged the reservoir, reduced porosity, and resulted in poor connectivity.

5.2.1. Early Diagenetic Stage

During the early diagenetic stage, the primary diagenetic transformations include the mechanical compaction, precipitation of calcite, dolomite, and iron calcite, formation of anhydrite minerals, and dissolution of quartz particles. Particle contacts are mainly point-to-line contacts. The organic matter in the reservoir has entered the immature to semi-mature stage. The oxidation of humic organic matter in the reservoir, along with the generation of acidic fluids, contributes to the formation of secondary dissolution pores, which, along with a small number of primary pores, constitute the reservoir space at this stage. The formation of secondary carbonate minerals such as calcite and dolomite is likely related to the dissolution and reprecipitation of primary carbonate clasts under acidic conditions.

5.2.2. Middle Diagenetic Stage

The diagenetic transformations during the middle diagenetic stage primarily include both mechanical and chemical compaction, the transformation of clay minerals such as kaolinite and smectite to illite, precipitation of carbonate minerals like calcite and dolomite, and dissolution of quartz, feldspar, rock fragments, and primary carbonate minerals. The organic matter in the reservoir has entered the mature to high-mature stage. The generation of organic acids and other substances promotes further dissolution, while the dissolution of potassium feldspar and other substances contributes to the illitization of smectite [43,44]. The dissolution of feldspar and rock fragments also provides material for the formation of carbonate cement. The contact modes between mineral particles are primarily line-to-concave–convex and line-to-suture contacts. Secondary dissolution pores represent the main reservoir space in this stage.

5.3. Controlling Factors of Reservoir Physical Properties

Overall, the factors affecting the physical properties of the reservoir include rock mineral composition, diagenesis, and tectonic movement. These factors influence rock type, sorting, matrix content, compaction, dissolution, and other characteristics, which jointly affect the pore throat structure of the reservoir and determine its performance.

Diagenesis plays a dominant role in the evolution of pore throat structure. The study presented in this paper shows that the strata in the Tengger and Arshan formations have reached the middle diagenetic stage. During deep burial, strong compaction leads to close contact between particles, significantly reducing primary porosity. Carbonate cements (calcite, dolomite), siliceous cements, and other cements block pores, further decreasing permeability. Secondary pores can form due to the dissolution of feldspar and rock fragments by multi-stage acidic fluids; however, the recementation of dissolution products (such as siliceous and carbonate minerals) counteracts some of the pore volume increase.

Sedimentary facies belt is also an important factor affecting reservoir physical properties. Taking the sedimentary facies divided by well S1 as an example, the deep lake and semi-deep lake facies of K_1a_2 are mainly fine-grained argillaceous deposits, with well-sorted particles but a high content of heterogeneities, poor physical properties, and they are rich in organic matter. They are the main source of rock sections, and the organic acids formed during the diagenetic evolution are conducive to the dissolution. In K_1t, the delta

deposits are mainly siltstone with relatively uniform pore structure, which is a favorable reservoir section. Relatively good connectivity is conducive to the migration of diagenetic fluid and plays a positive role in the dissolution. In addition, different substances are affected differently in the diagenetic process. For example, quartz has strong compressive compactness and stability, while feldspar is more sensitive to mechanical compaction and prone to alteration. Moreover, the composition of rock cuttings is complex; there are many unstable minerals, and the compressive compactness is weak and prone to dissolution and cementation. The sedimentary facies belt controls the physical properties of the reservoir by affecting the material composition of the reservoir.

Previous studies indicate that the Lower Cretaceous strata in the study area have undergone significant uplift, with a denudation thickness of up to 700 m [14]. The strong tectonic movement has led to the development of fractures within the reservoir, enhancing its seepage capacity.

According to high-pressure mercury injection (HPMI) experiments, the tight sandstone reservoirs in the study area are classified into three types of pore throat structures, each corresponding to different pore throat distributions. This study suggests that the pore throat structures of these reservoirs are mainly controlled by the rock material composition. Specifically, Type 1 reservoirs exhibit good sorting and the largest pore throat radii; Type 2 reservoirs have poor sorting but some large pore throat radii; and Type 3 reservoirs, though well sorted, feature the smallest pore throat radii and the worst physical properties (Figure 9). The reservoir spaces of these three types are dominated by secondary dissolution pores.

The correlation between pore throat structure and depth for the different types of reservoirs is weak (Table 2). The study shows that differences in reservoir spaces among these types are influenced by sedimentary components. Different clastic compositions have varying resistance to mechanical compaction and chemical stability, resulting in distinct diagenetic characteristics for rocks with different clastic compositions. The average composition of terrigenous clasts in the tight sandstone reservoir samples includes 44.3% rock fragments, 34.6% quartz, and 21.2% feldspar. A higher content of rock fragments, which contain more plastic particles, weakens the rock's resistance to compaction, hindering the preservation of primary pores. Conversely, quartz and other chemically stable particles impede the formation of secondary pores, while feldspar and other less chemically stable particles promote the formation of secondary pores. The different sedimentary components of sandstone are affected differently by compaction and cementation, influencing the distribution of residual primary intergranular pores. This, in turn, affects the strength of dissolution and cementation, leading to variations in pore throat structure and the physical properties of the reservoir. Different pore throat models were analyzed based on these research results (Figure 10).

6. Conclusions

The conclusions of this study are as follows:

1. The Lower Cretaceous sandstone in the Baibei Sag is primarily feldspathic lithic sandstone. The clastic particles are mainly composed of 44.3% rock fragments, 34.6% quartz, and 21.2% feldspar. The average content of clay minerals is 19.7%, with illite (69.3%) and I/S (12.7%) as the dominant minerals, and smaller amounts of chlorite (10.9%) and kaolinite (7.2%). The content of smectite is very low.
2. The effective porosity of the Tengger Formation sandstone reservoir is 3.3%, with an average permeability is 0.01×10^{-3} μm^2. For the Aershan Formation sandstone reservoir, the average effective porosity is 0.86%, with an average permeability of 0.05×10^{-3} μm^2. Both the Tengger and Aershan formations are classified as tight

sandstone reservoirs, and the reservoir space is primarily dominated by dissolution pores.

3. Three types of pore throat structures (HPMI curve: Type 1, Type 2, and Type 3) were identified, corresponding to different pore throat radius distributions (RCP curve: Type 1, Type 2, and Type 3). The pore throat structures of these three types are mainly controlled by mineral composition. And the pore models for different types of reservoirs have been established.
4. The maximum burial depth of the Aershan formation reached 2850 m, and the porosity rapidly decreased due to strong compaction. In addition, cementation dominated by carbonate minerals further reduces porosity. The fine-grained argillaceous deposits of deep lake and semi-deep lake facies in K_1a_2 and other mudstone intercalations formed the organic acid fluid in the evolution process. The organic acid fluid promoted the dissolution and formed the main reservoir space in the study area. The early tectonic fractures in the study area were filled with calcite, and the residual small-scale fractures played a positive role in material migration. Combined with the burial history and organic matter evolution characteristics, the diagenetic evolution sequence of the lower Cretaceous sandstone reservoir is established. The lower Cretaceous Tengger Formation and Arshan Formation reservoirs have entered the middle diagenetic stage A.

For the further development of this research, it is recommended to apply machine learning algorithms to improve the data analytics of core lab results.

Author Contributions: Writing—original draft, Data curation, H.T.; Supervision, Project administration, Methodology, Funding acquisition, Z.R.; Investigation, K.Q. and J.L.; Methodology, S.G. and Z.H.; Formal analysis, J.Y. and L.Z. All authors have read and agreed to the published version of the manuscript.

Funding: This research is funded by the National Natural Science Foundation of China, grant No. 42272152.

Data Availability Statement: Data are contained within the article.

Conflicts of Interest: The authors declare no conflicts of interest.

References

1. Xing, Y.; Zhang, Y.; Jiang, S.; Dong, X.; Wang,Y.; Wang, H.; Xu, Y. Characteristics and distribution of oil and gas reservoirs in the Wulanhua Sag of the Erlian Basin. *China Pet. Explor.* **2020**, *25*, 68.
2. Dou, L.; Chang, L. Fault linkage patterns and their control on the formation of the petroleum systems of the Erlian Basin, Eastern China. *Mar. Pet. Geol.* **2003**, *20*, 1213–1224. [CrossRef]
3. Si, W.; Hou, D.; Cao, L. Characterization of Crude Oil, Formation Water, and Fluid Inclusions of Hydrocarbon-Bearing Strata and Their Hydrocarbon Geological Significance in the Wuliyasitai Southern Sub-Sag of the Erlian Basin, China. *ACS Omega* **2023**, *8*, 29060–29082. [CrossRef] [PubMed]
4. Li, L.; Tang, D.; Xu, H.; Tao, S.; Chen, S.; Tang, S.; Yao, H. Coalbed methane geology and exploration potential in large, thick, low-rank seams in the Bayanhua Sag of the Erlian Basin, northern China. *Energy Explor. Exploit.* **2022**, *40*, 995–1022. [CrossRef]
5. Sun, F.; Li, W.; Sun, Q.; Sun, B.; Tian, W.; Chen, Y.; Chen, Z. Low-rank coalbed methane exploration in Jiergalangtu Sag, Erlian Basin. *Acta Pet. Sin.* **2017**, *38*, 485.
6. Bonnetti, C.; Malartre, F.; Huault, V.; Cuney, M.; Bourlange, S.; Liu, X.; Peng, Y. Sedimentology, stratigraphy and palynological occurrences of the late cretaceous Erlian formation, Erlian Basin, Inner Mongolia, People's Republic of China. *Cret. Res.* **2014**, *48*, 177–192. [CrossRef]
7. Chen, G.; Wang, T.; Li, L.; Li, S.; Li, J. Characteristics of a sublacustrine fan in a half-graben rift lake basin and its petroleum prospects: Case study on the second member of the Tenggeer Formation, Saihantala Sag, Erlian Basin. *Pet. Explor. Dev.* **2010**, *37*, 63–69. [CrossRef]
8. Wang, S.; Shao, L.; Wang, D.; Sun, Q.; Sun, B.; Lu, J. Sequence stratigraphy and coal accumulation of Lower Cretaceous coal-bearing series in Erlian Basin, northeastern China. *AAPG Bull.* **2019**, *103*, 1653–1690. [CrossRef]

9. Ren, J.; Tamaki, K.; Li, S.; Junxia, Z. Late Mesozoic and Cenozoic rifting and its dynamic setting in Eastern China and adjacent areas. *Tectonophysics* **2002**, *344*, 175–205. [CrossRef]
10. Wang, P.J.; Mattern, F.; Didenko, N.A.; Zhu, D.F.; Singer, B.; Sun, X.M. Tectonics and cycle system of the Cretaceous Songliao Basin: An inverted active continental margin basin. *Earth-Sci. Rev.* **2016**, *159*, 82–102. [CrossRef]
11. Gao, Y. Hydrocarbon accumulation conditions research and favorable zones prediction of Baibei Sag in Erlian Basin. *Pet. Geol. Eng.* **2015**, *29*, 38–41.
12. Zheng, L.W.; Dong, S.N.; Lin, J.; Liang, D.Y.; Hou, J.; Qiu, W.B. Characteristics and distribution patterns of the Tengger Formation reservoir in Baibei Sag of Erlian Basin. *Sci. Technol. Eng.* **2019**, *19*, 141–150.
13. Bai, X.Y.; Liu, H.C.; Li, K.S.; Chen, Z.J.; Han, C.C. Geologic characteristics and petroleum exploration potential of Baibei Sag in Erlian Basin. *J. Yanan Univ.* **2016**, *35*, 89–92.
14. Liu, H.; Ren, J.; Lyu, J.; Lyu, X.; Feng, Y. Hydrocarbon source rock evaluation of the Lower Cretaceous system in the Baibei Depression, Erlian Basin. *Energy Explor. Exploit.* **2018**, *36*, 355–372. [CrossRef]
15. Li, J.H.; Yu, L.; Shuai, J. The geochemical characteristics of source rocks in Baibei Depression of Erlian Basin. *Ground Water* **2016**, *38*, 248–250.
16. Olson, J.E.; Laubach, S.E.; Lander, R.H. Natural fracture characterization in tight gas sandstones: Integrating mechanics and diagenesis. *AAPG Bull.* **2009**, *93*, 1535–1549. [CrossRef]
17. Henares, S.; Caracciolo, L.; Cultrone, G.; Fernández, J.; Viseras, C. The role of diagenesis and depositional facies on pore system evolution in a Triassic outcrop analogue (SE Spain). *Mar. Pet. Geol.* **2014**, *51*, 136–151. [CrossRef]
18. Farrell, K.M.; Harris, W.B.; Mallinson, D.J.; Culver, S.J.; Riggs, S.R.; Wehmiller, J.F.; Moore, J.P.; Self-Trail, J.M.; Lautier, J.C. Graphic Logging for Interpreting Process-Generated Stratigraphic Sequences and Aquifer/Reservoir Potential: With Analog Shelf to Shoreface Examples from the Atlantic Coastal Plain Province, USA. *J. Sediment. Res.* **2013**, *83*, 723–745. [CrossRef]
19. Law, B.E.; Curtis, J.B. Introduction to unconventional petroleum systems. *AAPG Bull.* **2002**, *86*, 1851–1852.
20. Zou, C.; Tao, S.; Han, W.; Zhao, Z.; Ma, W.; Li, C.; Bai, B.; Gao, X. Geological and geochemical characteristics and exploration prospect of coal-derived tight sandstone gas in China: Case study of the Ordos, Sichuan, and Tarim Basins. *Acta Geol. Sin. Engl. Ed.* **2018**, *92*, 1609–1626. [CrossRef]
21. Li, M.; Guo, Y.; Li, Z.; Wang, H. The diagenetic controls of the reservoir heterogeneity in the tight sand gas reservoirs of the Zizhou Area in China's east Ordos Basin: Implications for reservoir quality predictions. *Mar. Pet. Geol.* **2020**, *112*, 104088. [CrossRef]
22. Beig, M.S.; Lüttge, A. Albite dissolution kinetics as a function of distance from equilibrium: Implications for natural feldspar weathering. *Geochim. Cosmochim. Acta* **2006**, *70*, 1402–1420. [CrossRef]
23. Crundwell, F.K. On the mechanism of the dissolution of quartz and silica in aqueous solutions. *ACS Omega* **2017**, *2*, 1116–1127. [CrossRef]
24. Higgs, K.E.; Zwingmann, H.; Reyes, A.G.; Funnell, R.H. Diagenesis, porosity evolution, and petroleum emplacement in tight gas reservoirs, Taranaki Basin, New Zealand. *J. Sediment. Res.* **2007**, *77*, 1003–1025. [CrossRef]
25. Mørk, M.B.E. Diagenesis and quartz cement distribution of low-permeability Upper Triassic–Middle Jurassic reservoir sandstones, Longyearbyen CO_2 lab well site in Svalbard, Norway. *AAPG Bull.* **2013**, *97*, 577–596. [CrossRef]
26. Nabawy, B.S.; Rochette, P.; Géraud, Y. Petrophysical and magnetic pore network anisotropy of some cretaceous sandstone from Tushka Basin, Egypt. *Geophys. J. Int.* **2009**, *177*, 43–61. [CrossRef]
27. Lai, J.; Wang, G.; Cai, C.; Fan, Z.; Wang, S.; Chen, J.; Luo, G. Diagenesis and reservoir quality in tight gas sandstones: The fourth member of the Upper Triassic Xujiahe Formation, Central Sichuan Basin, Southwest China. *Geol. J.* **2018**, *53*, 629–646. [CrossRef]
28. *Chinese Standard SY/T 5368-2016*; Identification for Thin Section of Rocks. National Energy Administration: Beijing, China, 2016.
29. *Chinese Standard SY/T 5163-2010*; Analysis Method for Clay Minerals and Ordinary Non-Clay Minerals in Sedimentary Rocks by the X-Ray Diffraction. National Energy Administration: Beijing, China, 2010.
30. *Chinese Standard SY/T 5346-2005*; Rock Capillary Pressure Measurement. National Development and Reform Commission: Beijing, China, 2005.
31. Houseknecht, D.W. Assessing the relative importance of compaction processes and cementation to reduction of porosity in sandstones. *AAPG Bull.* **1987**, *71*, 633–642.
32. Tobin, R.C.; McClain, T.; Lieber, R.B.; Ozkan, A.; Banfield, L.A.; Marchand, A.M.; McRae, L.E. Reservoir quality modeling of tight-gas sands in Wamsutter field: Integration of diagenesis, petroleum systems, and production data. *AAPG Bull.* **2010**, *94*, 1229–1266. [CrossRef]
33. Athy, L.F. Density, porosity, and compaction of sedimentary rocks. *AAPG Bull.* **1930**, *14*, 1–24.
34. Olivarius, M.; Weibel, R.; Hjuler, M.L.; Kristensen, L.; Mathiesen, A.; Nielsen, L.H.; Kjøller, C. Diagenetic effects on porosity–permeability relationships in red beds of the Lower Triassic Bunter Sandstone Formation in the North German Basin. *Sediment. Geol.* **2015**, *321*, 139–153. [CrossRef]

35. Cao, B.; Luo, X.; Zhang, L.; Sui, F.; Lin, H.; Lei, Y. Diagenetic evolution of deep sandstones and multiple-stage oil entrapment: A case study from the Lower Jurassic Sangonghe Formation in the Fukang Sag, central Junggar Basin (NW China). *J. Pet. Sci. Eng.* **2017**, *152*, 136–155. [CrossRef]
36. Xu, N.; Qiu, L.; Eriksson, K.A.; Klyukin, Y.I.; Wang, Y.; Yang, Y. Influence of detrital composition on the diagenetic history of tight sandstones with implications for reservoir quality: Examples from the Permian Xiashihezi Formation and Carboniferous Taiyuan Formation, Daniudi gas field, Ordos Basin, China. *Mar. Pet. Geol.* **2017**, *88*, 756–784. [CrossRef]
37. Dutton, S.P. Calcite cement in Permian deep-water sandstones, Delaware Basin, west Texas: Origin, distribution, and effect on reservoir properties. *AAPG Bull.* **2008**, *92*, 765–787. [CrossRef]
38. Loyd, S.J.; Corsetti, F.A.; Eiler, J.M.; Tripati, A.K. Determining the diagenetic conditions of concretion formation: Assessing temperatures and pore waters using clumped isotopes. *J. Sediment. Res.* **2012**, *82*, 1006–1016. [CrossRef]
39. Wang, J.; Cao, Y.; Liu, K.; Liu, J.; Xue, X.; Xu, Q. Pore fluid evolution, distribution and water-rock interactions of carbonate cements in red-bed sandstone reservoirs in the Dongying Depression, China. *Mar. Pet. Geol.* **2016**, *72*, 279–294. [CrossRef]
40. Salem, A.M.; Morad, S.; Mato, L.F.; Al-Aasm, I.S. Diagenesis and reservoir-quality evolution of fluvial sandstones during progressive burial and uplift: Evidence from the Upper Jurassic Boipeba Member, Recôncavo Basin, Northeastern Brazil. *AAPG Bull.* **2000**, *84*, 1015–1040.
41. Schmid, S.; Worden, R.H.; Fisher, Q.J. Diagenesis and reservoir quality of the Sherwood Sandstone (Triassic), Corrib field, Slyne basin, west of Ireland. *Mar. Pet. Geol.* **2004**, *21*, 299–315. [CrossRef]
42. Harris, N.B. Low-porosity haloes at stylolites in the feldspathic Upper Jurassic Ula sandstone, Norwegian North Sea: An integrated petrographic and chemical mass-balance approach. *J. Sediment. Res.* **2006**, *76*, 444–459. [CrossRef]
43. Berger, G.; Lacharpagne, J.C.; Velde, B.; Beaufort, D.; Lanson, B. Kinetic constraints on illitization reactions and the effects of organic diagenesis in sandstone/shale sequences. *Appl. Geochem.* **1997**, *12*, 23–35. [CrossRef]
44. Chuhan, F.A.; Bjørlykke, K.; Lowrey, C. The role of provenance in illitization of deeply buried reservoir sandstones from Haltenbanken and north Viking Graben, offshore Norway. *Mar. Pet. Geol.* **2000**, *17*, 673–689. [CrossRef]
45. Sanjuan, B.; Girard, J.P.; Lanini, S.; Bourguignon, A.; Brosse, E. Geochemical modelling of diagenetic illite and quartz cement formation in Brent sandstone reservoirs: Example of the Hild Field, Norwegian North Sea. *Clay Miner. Cem. Sandstones* **1999**, *34*, 425–452.
46. Henares, S.; Caracciolo, L.; Viseras, C.; Fernández, J.; Yeste, L.M. Diagenetic constraints on heterogeneous reservoir quality assessment: A Triassic outcrop analog of meandering fluvial reservoirs. *AAPG Bull.* **2016**, *100*, 1377–1398. [CrossRef]
47. Saïag, J.; Brigaud, B.; Portier, É.; Desaubliaux, G.; Bucherie, A.; Miska, S.; Pagel, M. Sedimentological control on the diagenesis and reservoir quality of tidal sandstones of the Upper Cape Hay Formation (Permian, Bonaparte Basin, Australia). *Mar. Pet. Geol.* **2016**, *77*, 597–624. [CrossRef]
48. Oluwadebi, A.G.; Taylor, K.G.; Dowey, P.J. Diagenetic controls on the reservoir quality of the tight gas Collyhurst sandstone formation, Lower Permian, East Irish Sea Basin, United Kingdom. *Sediment. Geol.* **2018**, *371*, 55–74. [CrossRef]
49. Morad, S.; Ketzer, J.M.; De Ros, L.F. Spatial and temporal distribution of diagenetic alterations in siliciclastic rocks: Implications for mass transfer in sedimentary basins. *Sedimentology* **2000**, *47*, 95–120. [CrossRef]
50. Surdam, R.C.; Crossey, L.J.; Hagen, E.S.; Heasler, H.P. Organic-inorganic interactions and sandstone diagenesis. *AAPG Bull.* **1989**, *73*, 1–23.
51. Lai, J.; Wang, G.; Chai, Y.; Xin, Y.; Wu, Q.; Zhang, X.; Sun, Y. Deep burial diagenesis and reservoir quality evolution of high-temperature, high-pressure sandstones: Examples from Lower Cretaceous Bashijiqike Formation in Keshen area, Kuqa depression, Tarim basin of China. *AAPG Bull.* **2017**, *101*, 829–862. [CrossRef]
52. Zou, C.N.; Tao, S.Z.; Hui, Z.; Zhang, X.X.; He, D.B.; Zhou, C.M.; Wang, L.; Wang, X.S.; Li, F.H.; Zhu, R.K.; et al. Genesis, classification, and evaluation method of diagenetic facies. *Pet. Explor. Dev.* **2008**, *35*, 526–540. [CrossRef]
53. Giles, M.R. Mass transfer and problems of secondary porosity creation in deeply buried hydrocarbon reservoirs. *Mar. Pet. Geol.* **1987**, *4*, 188–204. [CrossRef]
54. Mozley, P.S.; Heath, J.E.; Dewers, T.A.; Bauer, S.J. Origin and heterogeneity of pore sizes in the Mount Simon Sandstone and Eau Claire Formation: Implications for multiphase fluid flow. *Geosphere* **2016**, *12*, 1341–1361. [CrossRef]
55. Wilkinson, M.; Darby, D.; Haszeldine, R.S.; Couples, G.D. Secondary porosity generation during deep burial associated with overpressure leak-off: Fulmar Formation, United Kingdom Central Graben. *AAPG Bull.* **1997**, *81*, 803–813.
56. *Chinese Standard SY/T 5477-2003*; The Division of Diagenetic Stages in Clastic Rocks. State Economic and Trade Commission: Beijing, China, 2003.

Disclaimer/Publisher's Note: The statements, opinions and data contained in all publications are solely those of the individual author(s) and contributor(s) and not of MDPI and/or the editor(s). MDPI and/or the editor(s) disclaim responsibility for any injury to people or property resulting from any ideas, methods, instructions or products referred to in the content.